



## Feasibility study of a steel-UHPFRC hybrid tower for offshore wind turbines

Chao Chen<sup>a</sup>, Xiujiang Shen<sup>a,b,\*</sup>, Zheng Zhou<sup>a</sup>, Xugang Hua<sup>a</sup>

<sup>a</sup> College of Civil Engineering, Hunan University, Changsha, China

<sup>b</sup> Sustainable Materials, VITO, Boeretang 200, 2400, Mol, Belgium

### ARTICLE INFO

Handling Editor: Prof. A.I. Incecik

#### Keywords:

Offshore wind turbine  
UHPFRC  
Hybrid tower  
Fatigue life prediction  
Ultimate resistance

### ABSTRACT

A steel-ultra high performance fibre reinforced composites (steel-UHPFRC) hybrid tubular tower structure ( $\geq 100\text{m}$ ) is proposed and its feasibility to support an offshore wind turbine (OWT) with a 10 MW rotor is investigated in this paper. The hybrid tower combines a reinforced UHPFRC tube at the bottom and a steel tube at the top. Two numerical models are established to calculate the ultimate and fatigue loads for the hybrid tower and a standard steel tube tower as a reference. A simplified method is proposed to estimate the ultimate strength of the reinforced UHPFRC tube section, while a method based on the S–N curves is used to check its fatigue strength. It is found that the hybrid tower can satisfy design requirements and has a much longer fatigue life compared to the reference steel tower. Furthermore, the total material cost of the hybrid tower is found to be only 58% of that of the reference steel tower, while the masses of these two towers are kept close.

### 1. Introduction

Offshore wind has emerged as a new source of renewable energy, and its development now is recognized to be essential for the climate neutrality target at the horizon of 2050 (Musial et al., 2022). Over 315 GW of new offshore wind capacity is expected globally in the following decade (2022–2031), bringing the total offshore wind capacity to 370 GW in 2031 (GWEC, 2022). Nowadays, the overall trend worldwide is to increase the wind turbine power capacity by placing wind turbines at higher elevations for higher wind velocities and longer energy harvesting time, which inevitably leads to increasing height of the support structures. The average hub height for offshore wind turbines is expected to grow from 100 m in 2016 to 150 m in 2035 (Musial et al., 2022). In this context, the design of support structure for tall wind turbines faces new technical challenges from the larger wind and wave loads caused by increasing rotor sizes and tower diameters, very high loading cycles ( $>10^9$ ) during design service life (usually 20–25 years) and corrosion in aggressive marine environment.

At present, most support structures for OWTs are made of steel, which are generally vulnerable to fatigue damage and corrosion, resulting in high maintenance cost and limited design life (Price and Figueira, 2017). On the other hand, recent studies highlighted the potential benefits of using concrete for OWTs, considering that concrete structures have lower construction cost and less maintenance requirement than steel structures (Mathern et al., 2021). However, the concrete

structure requires more complex production process and quality control, involving labour-intensive and time-consuming construction activities (e.g., reinforcement placing, formworks, concrete casting and curing, post-stressing). Another issue with concrete structures is their vulnerability to fatigue and thus cracks, leaving steel reinforcements at high risk of corrosion due to chloride penetration from sea water in concrete. Therefore, increasing the typical steel or concrete support structures to new heights is neither straightforward nor cost effective in terms of technical and practical perspectives. To overcome those challenges, the technical innovation in materials combined with structural optimization is essential.

UHPFRC technology can become a mainstream solution for the problems and challenges mentioned above. Typically, UHPFRC have a compressive strength of 150–200 MPa, a tensile strength of 8–15 MPa, a strain hardening domain of 1–2%, and a very low capillary absorption, generally 5 times smaller than that of normal concrete prescribed for severe exposure class (Shen and Brühwiler, 2020a; Chen et al., 2018). Furthermore, UHPFRC has a fatigue endurance limit up to multimillion cycles under both tensile and compressive fatigue loads (Shen and Brühwiler, 2020b; Makita and Brühwiler, 2014a; Loroux, 2018). These appealing characteristics equip UHPFRC with the better capacity to improve the effectiveness, durability and sustainability of new or existing structures, which has been demonstrated by numerous recent successful structural applications (Brühwiler, 2020; Benjamin et al., 2020).

\* Corresponding author. Sustainable Materials, VITO, Boeretang 200, 2400, Mol, Belgium.

E-mail address: [xiujiang.shen@vito.be](mailto:xiujiang.shen@vito.be) (X. Shen).

UHPFRC, hence, is a suitable material to construct support structures for tall OWTs, which are usually exposed to harsh marine environment and subjected to highly fluctuating loads. However, very limited studies about application of UHPFRC on wind turbine structure can be found in the literature, to the best of the authors' knowledge. Most of them were focused on onshore wind turbines (Jammes, 2009; Jammes et al., 2013; Lewin, 2010; Wu et al., 2013; Sritharan and Schmitz, 2013; Toader et al.), while none of them were related to tall OWTs. Toader et al. (Toader et al.) proposed a segmented structure made of UHPFRC with prestressed tendons for onshore wind turbine towers, which can save up to 50% material compared to a prestressed concrete tower cast in situ. Similarly, an UHPFRC shell tower structure as proposed by Sritharan et al. (Sritharan and Lewin, 2015) used only 31.9% of the materials used in prestressed concrete design, and its weight was comparable to that of a steel tower. And it was indicated that the fatigue limit state was never dominated by the UHPFRC shell, but the steel tendons inside. Recently, Ma et al. (Ma and Yang, 2020) studied the feasibility of an UHPFRC-filled double skin steel tubular structure as monopile foundation for a 5 MW OWT. It was reported that the horizontal load at mudline and the total material cost for the proposed hybrid monopile can be reduced by up to 41.8% and 20.7% compared with traditional steel tubular structure, respectively.

Thus, aiming at robust, durable and economic support structure for tall OWTs, this paper originally proposes a steel-UHPFRC hybrid tower

structure. It is expected to address the aforementioned problems and challenges when the OWTs keep scaling up, by benefiting from the hybrid-tower concept and appealing properties of UHPFRC. Afterwards, a comprehensive feasibility study of this hybrid tower with height of 149 m is presented regarding the ultimate and fatigue limit state of the reinforced UHPFRC tube under various operating conditions. Results are also compared to those obtained from a reference standard steel tower.

## 2. Concept of the hybrid tower

As illustrated in Fig. 1(a), the proposed steel-UHPFRC hybrid tower (the part above mudline) consists of a UHPFRC tube at the bottom and a steel tube at the top. The UHPFRC tube is assumed to be assembled by a series of precast UHPFRC arc segments circumferentially and vertically, as shown in Fig. 2. For the connection between UHPFRC arc segments, the conventional steel inner flanges imbedded on the sides of UHPFRC arc segments are applied firstly, then UHPFRC is cast in the joint to strengthen the connection and serves as protective layer for the steel flanges. It should be noted that the dovetail shape and extra steel rebars are used in the joint to further enhance the connection. The UHPFRC tube and the steel tube is assumed to be connected by a traditional flange. A better design of these connections is possible, but this is out of this paper's scope.

Compared with the traditional solution with a standard steel tower in

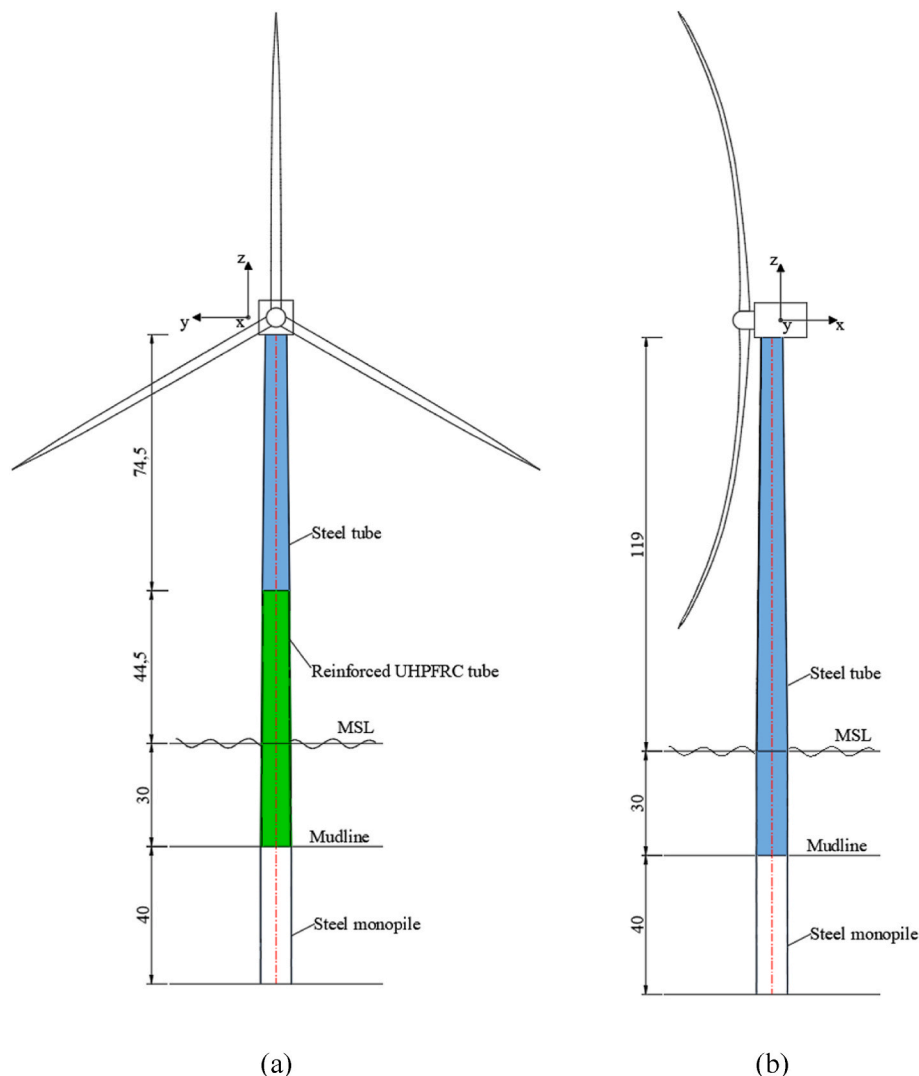


Fig. 1. Schematic illustration: (a) steel-UHPFRC hybrid tower for OWT; (b) reference steel tower (unit: m).

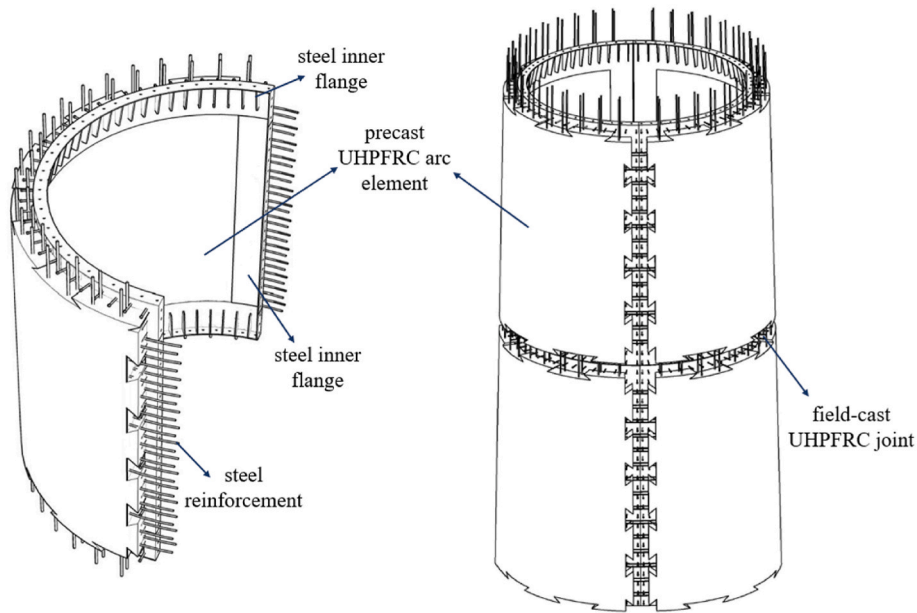


Fig. 2. Schematic illustration of precast UHPFRC arc segment and assembly of UHPFRC tube structure.

Fig. 1(b) for OWTs, the proposed steel-UHPFRC hybrid tower has following characteristics:

- 1) The appealing mechanical properties of UHPFRC in both tension and compression can be fully exploited in the OWT tower under various loading cases. The connection using steel inner flanges and cast-on-site UHPFRC joint can ensure the overall structure performance of tower. Additionally, with properly designed cross sections, the outstanding fatigue resistance of UHPFRC with apparent endurance limit of UHPFRC is expected to avoid the requirement of prestressing and largely reduce the amount steel reinforcement inside.
- 2) Owing to the extreme compactness and stain-hardening behaviour of UHPFRC, the water and chloride can hardly penetrate inside even in harsh marine environment, thus highly increasing the durability and extending the service life of tower structure.

- 3) The UHPFRC arc segments can be easily transported and assembled on-site using traditional methods. During the extended service life, the maintenance work can be largely simplified and reduced.

Therefore, considering as a more economic and robust structure, the proposed hybrid tower is a competitive solution for tall OWTs.

It should be mentioned that the purpose of this study is to preliminarily investigate the feasibility of the hybrid tower concept based on UHPFRC. Therefore, the connections between the reinforced UHPFRC segments and the connection between the UHPFRC tube and the steel tube are assumed to have higher strength compared to the monotonic tower, so the numerical modelling of the hybrid tower does not consider the influence of connections for simplicity.

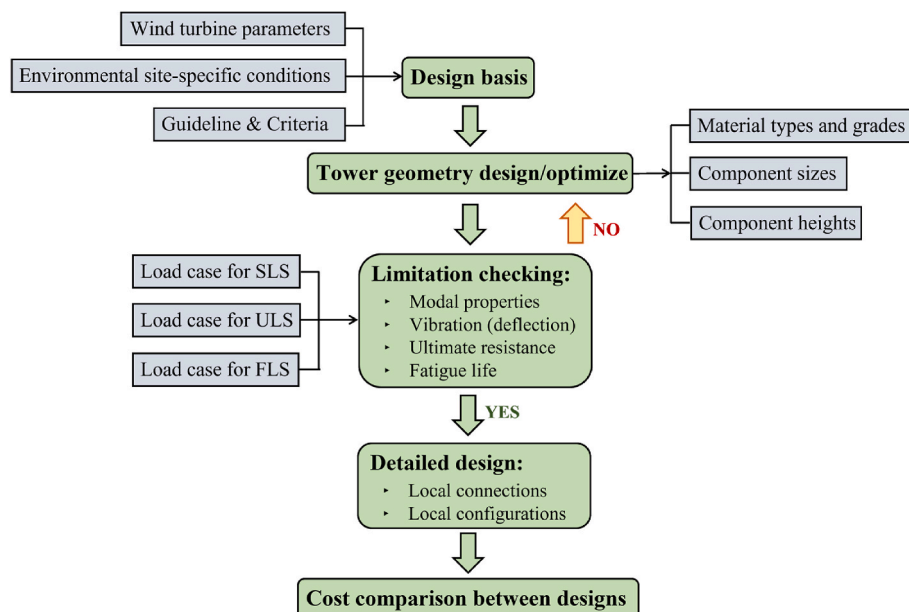


Fig. 3. Design procedure for wind turbine tower structure.

### 3. Analysis methods for the hybrid tower

#### 3.1. Overview

In general, the wind turbine tower structure can be designed following the iterative procedure as shown in Fig. 3. Similar approaches were adopted by different researchers (Damiani et al.; Peggar, 2017; Huang et al., 2022). Based on the design basis, a preliminary design is achieved firstly. This phase strongly relies on engineering judgement and past experience on tower structures and material properties. After the selection of load cases, the corresponding responses of the tower structure are determined and checked following the specific standards via finite element (FE) analysis and nonlinear structural analysis. This process is conducted iteratively until the structural and functional requirements are met by the finalized geometry of the proposed tower structure.

In the following subsections, the FE model for modal analysis and load-response analysis (static and dynamic), sectional analysis method for ultimate flexural resistance and damage analysis for fatigue life prediction of the overall tower structure are developed and described. Practically, a detailed failure analysis is very important for composite structures like the steel-UHPFRC tube proposed in the paper (Riccio et al., 2016; Shabani and Shabani, 2022; Zhai et al., 2023). However, this detailed analysis is out of this paper's scope and such analysis will be conducted in the future.

#### 3.2. Aeroelastic FE model

##### 3.2.1. Overview

Based on the authors' previous study (Chen et al., 2021), a fully coupled aeroelastic model is developed using MATLAB to determine the modal properties and dynamic responses of the hybrid tower. This aeroelastic model is a FE formulation including the blades, tower and monopile represented by soil springs lumped at the mudline. Compared to widely used wind turbine modelling software such as FAST (Jonkman and Buhl, 2005), this aeroelastic model benefits from the easy consideration of soil-structure interaction (SSI) and modelling the hybrid tower with high accuracy.

In the FE model, the tower and blades are modelled using three-dimensional Euler-Bernoulli beam elements. The numbers of beam elements for each single blade and tower are 37 and 25 respectively, and in total, 136 beam elements are used. A convergence study confirms that the beam element number is sufficient. Given the material and geometric properties of the beam elements, the equations of motion of the FE model are:

$$\mathbf{M}\ddot{\mathbf{u}} + (\mathbf{C}_{Struc} + \mathbf{C}_{Soil})\dot{\mathbf{u}} + \mathbf{K}\mathbf{u} = \mathbf{F}_{Wind} + \mathbf{F}_{Wave}, \quad (1)$$

where  $\mathbf{M}$ ,  $\mathbf{K}$  are the mass and stiffness matrices,  $\mathbf{C}_{Struc}$  and  $\mathbf{C}_{Soil}$  are the structural damping and soil damping matrices respectively,  $\mathbf{u}$  is the displacement vector,  $\mathbf{F}_{Wind}$  and  $\mathbf{F}_{Wave}$  are the wind force and wave force vectors. It should be noted that the stiffnesses of beam elements are directly obtained from tower geometries and materials' Young's moduli. So nonlinear material properties are not considered in this model. The structural damping and soil damping in this study are both assumed to be proportional Rayleigh damping. The total damping ratios due to the structural damping and soil damping are 2.0% according to (Chen and Duffour, 2018). The structural damping of a single blade was set to 0.48% according to (Bak et al.). The definition of the damping ratios is only for the first bending modes of the tower and the blade in the relevant directions. The hydrodynamic damping and aerodynamic damping of the tower are not included as their contributions are small compared to other damping sources (Chen and Duffour, 2018). The nacelle and hub are modelled using a lumped mass at the tower top, added to the mass matrix. For simplicity, the gravitational centre of the nacelle is located at the tower top, so that moments of inertia of the

nacelle about all axes are zero. Time domain analyses are conducted by implementing the numerical integration scheme HHT- $\alpha$ , which is a generalised version of the Newmark- $\beta$  method. The FE model was successfully verified against FAST in the authors' previous studies (Chen et al., 2021, 2023).

##### 3.2.2. Aerodynamic loading

The wind loading on the rotor is calculated by unsteady blade element momentum (BEM) theory with corrections (Hansen, 2015). The corrections adopted in the unsteady BEM code include Prandtl and Glauert corrections. Other corrections such as skew wake and dynamic wake corrections are not included in the unsteady BEM code for simplicity. The wind loading on the tower is calculated by the equation below:

$$F_{wind,tower} = \frac{1}{2}C_{dt}\rho_a Du_a^2, \quad (2)$$

where  $C_{dt}$  is a drag coefficient,  $\rho_a$  is the air density,  $D$  is the diameter of the tower and  $u_a$  is the wind velocity. The velocities caused by tower vibration were ignored as the tower vibration velocities are much smaller than the inflow wind speed.

A customised turbulent wind field generator is also coded in MATLAB to generate non-uniform turbulent inflow wind fields as the input to the unsteady BEM code. The Kaimal spectrum is used to generate the turbulent wind field, and its relevant parameters (e.g., coherence length parameters) are selected as recommended by IEC 61400-3 (International Electrotechnical et al.). The relationship between turbulence intensities and mean wind speeds at hub height is defined according to the normal turbulence model (NTM), where medium turbulence intensity (Category B) is assumed. The inflow wind velocities, the velocity caused by rotor rotation and the velocities caused by blade vibration are used as input to the unsteady BEM code. The unsteady code calculates the instantaneous local aerodynamic forces for all blade elements at every time step in the time integration.

##### 3.2.3. Hydrodynamic loading

Following Morison's equation (Veldkamp and Tempel, 2005), the wave force combines a viscous drag force and an inertia force:

$$F_{wave} = \frac{1}{2}\rho_w DC_d |\dot{u}_w| \dot{u}_w + \frac{\pi}{4}\rho_w D^2 C_m \ddot{u}_w, \quad (3)$$

where  $\dot{u}_w$  and  $\ddot{u}_w$  are the velocity and acceleration of water particles;  $C_d$  is the drag coefficient;  $D$  is the diameter of the tower between the mean sea level (MSL) and the mudline;  $C_m$  is the inertia coefficient and  $\rho_w$  is the density of water. Here  $C_d = 1$  and  $C_m = 2$  are chosen as recommended in (Shirzadeh et al., 2013). The velocities caused by monopile vibration are ignored in the wave loading calculation as the monopile vibration velocities are much smaller than the wave particle velocities.

The wave profile is irregular and obtained by the superposition of wave components following linear wave theory and JONSWAP spectrum (Hasselmann et al., 1973). For a particular frequency point  $f$ , the JONSWAP spectrum definition is given by

$$S_{JS} = S_{PM}(f) \bullet (1 - 0.287 \ln(\gamma)) \bullet \gamma^{\exp\left[\frac{(f-f_p)^2}{2\sigma^2 f_p^2}\right]}, \quad (4)$$

and

$$S_{PM}(f) = 0.3125 H_s^2 T_p \left(\frac{f}{f_p}\right)^{-5} \exp\left[-1.25 \left(\frac{f}{f_p}\right)^{-4}\right]. \quad (5)$$

where  $f_p$  is the peak frequency defined as  $1/T_p$ , in which  $T_p$  is the peak wave period;  $H_s$  is the significant wave height;  $\gamma$  is the peak-shape parameter, which is assumed to be equal to 3.3 for the North Sea conditions according to (Hasselmann et al., 1973);  $\sigma$  is the spectral width

parameter. The wave elevation, velocity and acceleration time series can be obtained by summing wave components corresponding to different wave frequencies.

### 3.2.4. Soil structure interaction

The steel monopile is assumed to be surrounded by a single layer of sand in this study. The saturated soil weight is  $20 \text{ kN/m}^3$  and the internal friction angle is  $36^\circ$ . The SSI is modelled by a simplified method in which lumped springs at the mudline to accelerate the fatigue analysis. This method assumes a stiff monopile, and its stiffness coefficients are calculated based on the method described in (Darvishi-Alamouti et al., 2017; Wang et al., 2021). The lateral stiffness  $K_{uu}$ , rotational stiffness  $K_{\theta\theta}$  and cross-coupling stiffness  $K_{u\theta}$  are determined by

$$\begin{bmatrix} K_{uu} & K_{u\theta} \\ K_{u\theta} & K_{\theta\theta} \end{bmatrix} = \begin{bmatrix} \frac{1}{2}L_p^2 n_h & -\frac{1}{3}L_p^3 n_h \\ -\frac{1}{3}L_p^3 n_h & \frac{1}{4}L_p^4 n_h \end{bmatrix}, \quad (6)$$

where  $L_p$  is the length of the steel monopile;  $n_h$  is a coefficient of subgrade reaction constant with depth.  $n_h$  is taken as  $5000 \text{ kN/m}^3$  for medium dense sand according to (Wang et al., 2021). It is assumed that the top of the steel monopile is unable to move vertically and rotate around  $z$  axis.

### 3.3. Ultimate resistance

Under the dead loads and live loads, an extremely high bending moment is expected at the bottom part of the hybrid tower (Adhikari and Bhattacharya, 2012), where the reinforced UHPFRC tube should provide enough load-bearing capacity to transfer the loads to the foundation. Thus, a sectional analysis method considering the tensile behaviour of UHPFRC is proposed here to determine the ultimate resistance of reinforced UHPFRC section under ultimate limit state.

A reinforced UHPFRC tube section with a thickness of  $t$ , outer radius of  $R$  and inner radius of  $r$ , is plotted in Fig. 4. The reinforced UHPFRC section is separated into three zones marked by zone I, zone II, and zone III respectively. The widths of zone I and zone III are equal to section thickness  $t$ , while the width of zone II is equal to the inner diameter of the tube section. The origin of  $X$  and  $Y$  axes located at the centre and this section is divided into a number of partitions of an equal width of  $dh$ . An arbitrary partition is related a horizontal coordinate of  $x_i$ . A plane section assumption is made for this section after deformation, leading to a linear strain distribution along the section. Therefore, the tensile strain reaches its maximum value at the right end ( $X = R$ ). The total force in UHPFRC zone I is:

$$F_{U1} = \int_r^R \sqrt{R^2 - x_i^2} \cdot 2 \cdot \sigma_{Ui} \cdot dh. \quad (7)$$

The total force in UHPFRC zone II:

$$F_{U2} = \int_{-r}^r (\sqrt{R^2 - x_i^2} - \sqrt{r^2 - x_i^2}) \cdot 2 \cdot \sigma_{Ui} \cdot dh. \quad (8)$$

The total force in UHPFRC zone III:

$$F_{U3} = \int_{-R}^{-r} \sqrt{R^2 - x_i^2} \cdot 2 \cdot \sigma_{Ui} \cdot dh. \quad (9)$$

where  $\sigma_{Ui}$  is determined based on the stress-strain curve of UHPFRC either in tension or compression, and  $\epsilon_{Ui} = \frac{x_i + X_{n-n} - R}{X_{n-n}} \cdot \epsilon_{Utop}$ . The corresponding moments about the neutral line are:

$$M_{U1} = \int_r^R \sqrt{R^2 - x_i^2} \cdot 2 \cdot \sigma_{Ui} \cdot (x_i + X_{n-n} - R) \cdot dh, \quad (10)$$

$$M_{U2} = \int_{-r}^r (\sqrt{R^2 - x_i^2} - \sqrt{r^2 - x_i^2}) \cdot 2 \cdot \sigma_{Ui} \cdot (x_i + X_{n-n} - R) \cdot dh, \quad (11)$$

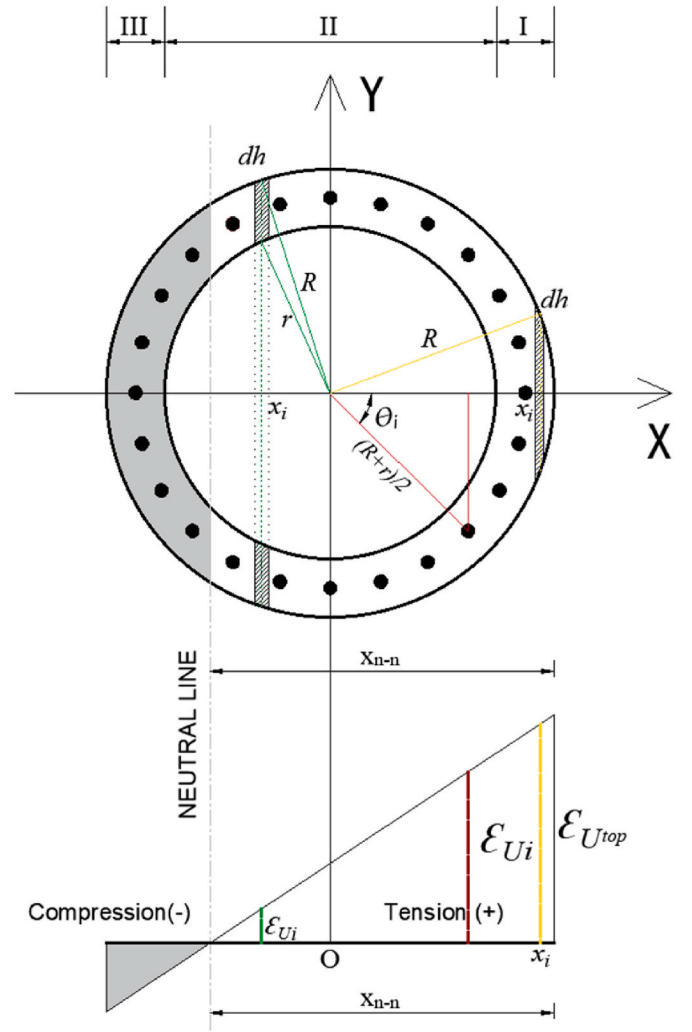


Fig. 4. Diagram for the ultimate resistance of a reinforced UHPFRC tube section.

$$M_{U3} = \int_{-R}^{-r} \sqrt{R^2 - x_i^2} \cdot 2 \cdot \sigma_{Ui} \cdot (x_i + X_{n-n} - R) \cdot dh. \quad (12)$$

The total force in steel rebars can be calculated by

$$F_S = \sum_{j=1}^{n_{bar}} \pi \cdot r_s^2 \cdot \sigma_{sj}, \quad (13)$$

where  $n_{bar}$  is the total number of steel rebars,  $r_s$  is the rebar radius.  $\sigma_{sj}$  is the stress for the  $j^{th}$  rebar corresponding to a strain  $\epsilon_{sj} = \frac{\frac{R+r}{2} \cdot \cos \theta_j + X_{n-n} - R}{X_{n-n}} \cdot \epsilon_{Utop}$ .  $\theta_j$  represents the angular position of the rebar. The corresponding total moment for rebars is:

$$M_S = \sum_{j=1}^{n_{bar}} \pi \cdot r_s^2 \cdot \sigma_{sj} \cdot \left( \frac{R+r}{2} \cdot \cos \theta_j + X_{n-n} - R \right). \quad (14)$$

For a given geometry, reinforcement (without prestress), and material properties, the resistance calculation is as follows:

1. Assume a value for the neutral line position  $X_{n-n}$ , as well as the maximum tensile strain at the right side of the UHPFRC section  $\epsilon_{Utop}$ ;
2. By trial and error, find the specific value of  $X_{n-n}$ , making  $F_{U1} + F_{U2} + F_{U3} + F_S = F_z$ , where  $F_z$  is the total vertical load applied on the section;

3. With the specific pair of  $(X_{n-n}, \varepsilon_{Utop})$ , calculate the total moment  $M_u = M_{U1} + M_{U2} + M_{U3} + M_S$ ;
4. Repeat steps 1 through 3, find the maximum value of  $M_u$ .

A material factor of 1.3 (Swiss Society of Engineers and Architects, 2016) is adopted for the ultimate strength calculation of the reinforced UHPFRC.

The ultimate strength of the steel tube section in the reference tower should also be estimated. A method based on (Uys et al., 2007) and DNVGL-RP-C202 (DNVGL, DNVGL-RP-C202, 2019) is developed to calculate the maximum moment the steel tube section can take given a known axial force. As the axial force in the steel tube section is mainly caused by gravity loading and does not fluctuate significantly due to the stochastic environmental loading, it is reasonable to assume a constant axial force when estimating the maximum moment. Details of the method which calculates the steel tube ultimate strength are provided in Appendix A. The methods to calculate the ultimate strengths of the reinforced UHPFRC tube section and the reference steel tube section were both coded in MATLAB.

### 3.4. Fatigue strength

Fatigue damage is quantified given the hotspot stresses for the tower structure with the S–N curves from corresponding materials. Currently, there is no widely accepted S–N curve for UHPFRC in tension due to the limited studies and experimental data. Similar to steel, UHPFRC shows a fatigue endurance limit, above which fatigue stress induces significant damage leading to fracture failure. Based on the study by Makita et al. (Makita and Brühwiler, 2014a), an endurance limit was determined at a stress level of  $S = \Delta\sigma_u/f_{Ute} = 0.7$  for undamaged UHPFRC under fatigue tension.  $\Delta\sigma_u$  is the stress range of UHPFRC. Comparable phenomenon was observed for UHPFRC under equi-biaxial tension from the authors' previous study (Shen and Brühwiler, 2020b). For the tensile fatigue behaviour of UHPFRC, the study by Makita (2014) provides the following S–N relationship:

$$S = \Delta\sigma_u/f_{Ute} = -0.085 \bullet \log N + 1.364. \quad (15)$$

Regarding the compressive fatigue behaviour of UHPFRC, an endurance limit is chosen as  $S = \Delta\sigma_u/f_{Ucu} = 0.65$ , according to the study from Loraux (2018). And the corresponding compressive S–N curve is:

$$S = \Delta\sigma_u/f_{Ucu} = -0.044 \bullet \log N + 0.981. \quad (16)$$

This tensile and compressive fatigue S–N curves for UHPFRC are

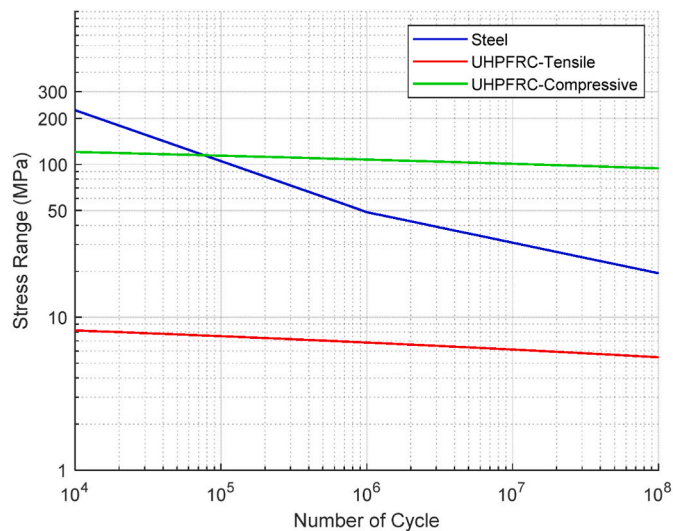


Fig. 5. Compressive and tensile fatigue S–N curves for UHPFRC; S–N curve for steel tube.

plotted in red and green in Fig. 5, respectively.

Furthermore, it was indicated experimentally that the tensile fatigue endurance limit in tension could be improved to a stress level that UHPFRC is in the strain-hardening domain with steel reinforcement (Makita and Brühwiler, 2014b). According to the study by Makita and Brühwiler (2014b), the fatigue behaviour of reinforced UHPFRC in a bridge deck is mainly dependent on UHPFRC in the early stage, but steel rebars predominantly determine the reinforced UHPFRC's fatigue behaviour in the middle and final stages. As the number of fatigue cycles increases, it was found that the stress gradually transfers from UHPFRC to steel rebars. Therefore, the final fatigue strength of reinforced UHPFRC is dependent on the rebars' ability to resist fatigue damages. As there is no experimental study for the fatigue behaviour of reinforced UHPFRC tube section under axial force and bending moment, the S–N curve obtained in (Makita and Brühwiler, 2014b) for rebars in a reinforced UHPFRC layer to strengthen a bridge deck slab was selected to evaluate the fatigue strength of the reinforced UHPFRC tube section. This S–N curve is given by

$$\log \Delta\sigma_r = -0.1 \bullet \log N + 2.86. \quad (17)$$

where  $\Delta\sigma_r$  is the stress range of rebar. This S–N curve is plotted in blue in Fig. 6, compared to the S–N curve for a single rebar.

For steel tube, the fatigue estimation can be based on widely used S–N curves for steel plates provided by the DNVGL code (DNV et al.). This S–N curve is defined by

$$\log N = \log \bar{a} - m \log \Delta\sigma_s \left( \frac{t_c}{t_{ref}} \right)^k \quad (18)$$

where  $N$  refers to the number of cycles to failure,  $\Delta\sigma_s$  is the stress range,  $m$  is the negative inverse slope of the S–N curve,  $\log \bar{a}$  is the intercept of  $\log N$  axis,  $t_{ref}$  is the reference thickness,  $t_c$  is the thickness through which a crack `bib_dnv_et_al` will most likely grow,  $k$  is the thickness exponent of fatigue strength. For a steel tube section below water, a S–N curve of class E is selected (Rezaei et al., 2018), which is plotted in blue in Fig. 5.

The hotspot stresses of the OWT tower structures have variable amplitudes due to fluctuating wind and wave loads. As a result, rainflow counting was used to bin the stress amplitudes into multiple stress levels and count the number of cycles in every stress bin. Given the S–N curves and the counted number of cycles, the total damage caused by every stress bin can be found and then added together to obtain the total damage via the widely used Palmgren-Miner sum rule. The total damage

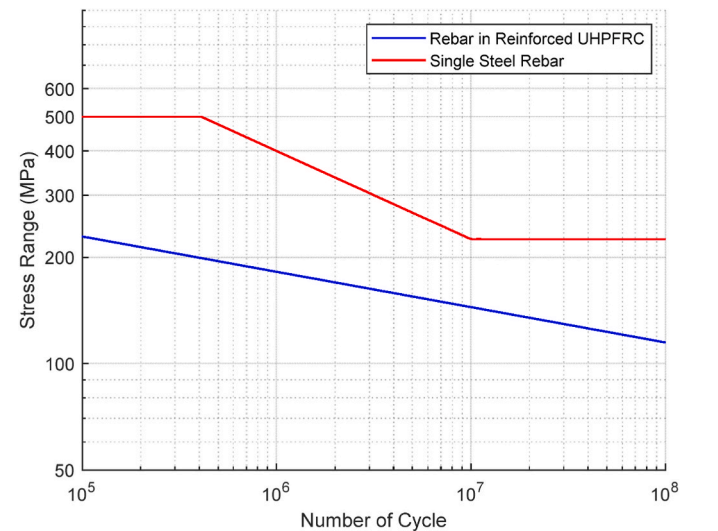


Fig. 6. Tensile fatigue S–N curves for rebars in reinforced UHPFRC and a single steel rebar.

index  $D$  can be expressed by

$$D = \sum_{i=1}^{N_c} \frac{n_i}{N_i}, \quad (19)$$

where  $n_i$  is the number of cycles in  $i^{th}$  stress bin,  $N_i$  is the number of cycles to fatigue failure for the nominal stress cycle amplitude  $i$ , and  $N_c$  is the total number of bins. A total damage index equal to 1 indicates the fatigue failure, so the fatigue life can be estimated by the damages obtained from 10 min simulations under different load conditions, by assuming that these simulated 10 min dynamic responses can reflect the long-term dynamic behavior of an OWT through its lifetime.

#### 4. Preliminary design of steel-UHPFRC hybrid tower

In order to validate the feasibility and competitiveness of the proposal, a steel-UHPFRC hybrid tower structure is designed accordingly to support a DTU 10 MW wind turbine (Bak et al.). In addition, a conventional steel tower with variable-section part above the MSL and constant-section part below the MSL following Yang et al. (2020) is used as reference. In the following subsections, the structural responses of the finalized hybrid tower structures are investigated and compared with reference.

##### 4.1. Geometric configuration

As shown in Fig. 1, both tower structures have top height of 119 m above the MSL, 30 m height in water depth, and 40-m steel monopile under the mudline as foundation. The soil around the steel monopile is assumed to be medium-dense sand. The basic parameters of the DTU 10 MW wind turbine and steel monopile are listed in Table 1. A coordinate system is defined in Fig. 1, where  $x$  and  $y$  axes point to the fore-aft (FA) and side-side (SS) directions respectively,  $z$  axis is vertically upward.

The length of the reinforced UHPFRC tube is designed as half of the total length of the hybrid tower above the mudline, and the upper steel tube is the same as that in the reference tower. Additionally, the outer diameter of the top section of the UHPFRC tube part is the same as the bottom section of the steel tube part for easy connection. The geometric characteristics of the hybrid tower and reference tower are presented in Table 2 and Table 3, respectively. The selection of the geometric properties follows the iteration process shown in Fig. 3, which results in very close estimated tower top displacements under the rated wind speed for these two towers. Although the way to select the geometric properties could not be optimal, it makes the two towers comparable in terms of stiffness.

##### 4.2. Materials and properties

The strain-hardening UHPFRC (fiber volume content  $\geq 3.0\%$  generally), which exhibits relatively robust mechanical properties, is used with the particular aim at exploiting the excellent tensile response of UHPFRC under both static and fatigue loading. The D500 steel rebars

**Table 1**  
Basic parameters for DTU 10 MW reference offshore wind turbine based on (Bak et al.; Yang et al., 2020).

Parameter	Value
Rated power (MW)	10
Cut-in/cut-out speeds (m/s)	4/25
Rated wind speed (m/s)	11.4
Rotor diameter (m)	178.3
Hub height (m)	119
Rotor nacelle assembly mass (t)	674
Steel monopile length (m)	40
Steel monopile diameter (m)	9
Steel monopile thickness (mm)	110

**Table 2**  
Geometric characteristics of the steel-UHPFRC hybrid tower.

Steel tube		UHPFRC tube	
Length (m)	74.5	Length (m)	74.5
Top diameter (m)	6.25	Top diameter (m)	7.97
Bottom diameter (m)	7.97	Bottom diameter (m)	9
Top thickness (mm)	35	Top thickness (mm)	300
Bottom thickness (mm)	54.7	Bottom thickness (mm)	400

**Table 3**  
Geometric characteristics of the reference steel tower.

Steel tube above MSL		Steel tube below MSL	
Length (m)	119	Length (m)	30
Top diameter (m)	6.25	Diameter (m)	9
Bottom diameter (m)	9	Top thickness (mm)	110
Top thickness (mm)	35		
Bottom thickness (mm)	66.5		

are used to reinforce UHPFRC with a reinforcement ratio of 1%, which is noticeably lower than that used in normal concrete wind turbine tower structure. It should be noted that no post-prestressing tendons are applied in the hybrid tower, which can largely simplify the construction on-site. The steel tube part in hybrid tower and reference tower are both made of steel S355. The main material properties used in the present study are listed in Table 4. In addition, the strain-stress relationships for UHPFRC and steel rebar are shown in Fig. 7, and their characteristic values are listed in Table 5.

##### 4.3. Load cases

To study the capacities of the hybrid tower against large environmental loads, it needs to define the critical environmental states and corresponding load cases to cover both operating and parked conditions. From structural perspective, tower loads can be mainly categorized into ultimate limit state (ULS) and fatigue limit state (FLS) cases, which are generally dominate the design of tower structure for OWTs. The load cases in present study are applied according to IEC 61400-3 OWT design standard (International Electrotechnical et al.), where design load case (DLC) 1.1 and DLC6.1 are selected for ULS analysis and DLC1.2 for FLS analysis as shown in Table 6. It should be noted that the extreme wind turbulence and severe waves, which lead to larger ultimate loads, are not considered here.

DLC1.1 considers the operation of OWT under normal turbulent winds and normal waves. The metocean data used here is based on the data provided in the paper by Velarde et al. (2020), as a comprehensive fatigue reliability study was conducted in (Velarde et al., 2020) considering both operational and parked conditions with carefully selected environmental load cases. For DLC1.1, the wind speeds  $V_w$  from

**Table 4**  
Material properties of UHPFRC and steel.

Reinforced UHPFRC tube		Steel tube	
UHPFRC	Rebar	Steel	Steel
Density (kg/m <sup>3</sup> )	2700	Density (kg/m <sup>3</sup> )	7850
Young's modulus (GPa)	48	Young's modulus (GPa)	200
Poisson's ratios	0.2	Poisson's ratios	0.3
Shear modulus (GPa)	20	Shear modulus (GPa)	76.9
Compressive strength (MPa)	150	Yield strength (MPa)	500
Tensile strength (MPa)	12	Yield strength (MPa)	355

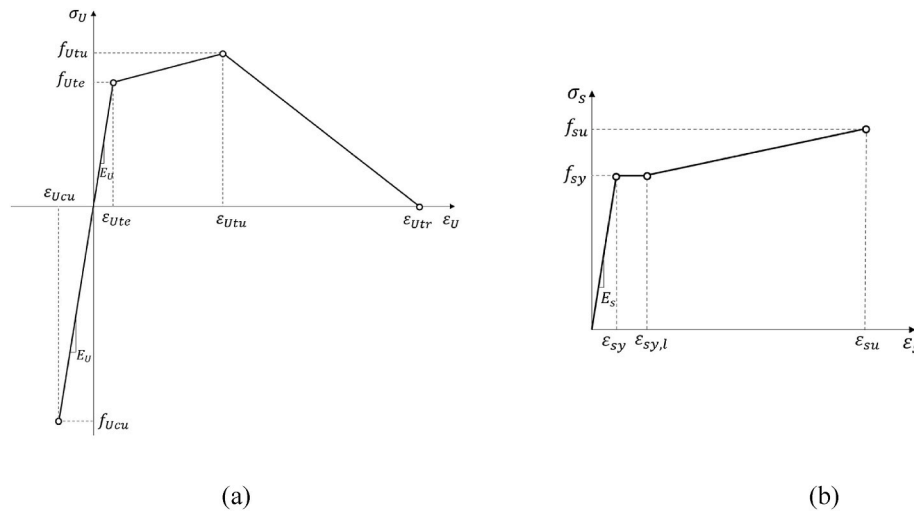


Fig. 7. Strain-stress relationship for UHPFRC (a) and steel rebar (b).

**Table 5**  
Characteristic stress and strain for UHPFRC and steel rebar.

UHPFRC		Steel rebar	
$f_{Ute}$ (MPa)	8	$f_{sy}$ (MPa)	500
$\epsilon_{Ute}$ (%)	0.0167	$\epsilon_{sy}$ (%)	0.25
$f_{Utu}$ (MPa)	12	$\epsilon_{sy,l}$ (%)	2.5
$\epsilon_{Utu}$ (%)	0.2	$f_{su}$ (MPa)	565
$\epsilon_{Utr}$ (%)	1	$\epsilon_{su}$ (%)	15
$f_{Ucu}$ (MPa)	150		
$\epsilon_{Ucu}$ (%)	0.3125		

5 m/s to 25 m/s in 2 m/s steps with the normal turbulent intensity  $I_n$  are listed in Table 7. For each wind speed, the corresponding peak wave period and significant wave height are picked for normal sea state and severe sea state, respectively. DLC6.1 considers idling or parked wind turbines subjected to extreme wind and wave loads with a 50-year return period. DLC6.1 is analysed under a reference wind speed of 45.8 m/s as provided in (Wang et al., 2021), with wind turbulence and wave parameters listed in the bottom of Table 7.

DLC1.2 corresponds to normal operation condition for fatigue analysis. The wind speeds from 5 m/s to 25 m/s (grouped into 2 m/s bins) with normal turbulence and normal sea state are applied. Furthermore, to determine the long-term joint distribution of the wind and wave conditions, a two-parameter Weibull distribution is used:

$$f(v) = \frac{k}{A} \left(\frac{v}{A}\right)^{k-1} \exp\left(-\left(\frac{v}{A}\right)^k\right), \quad (20)$$

where  $A$  is a scale parameter and  $k$  is a shape parameter. According to (International Electrotechnical et al.), for a standard metocean condition,  $k = 2$  and  $A = 2v_{ave}/\sqrt{\pi}$ , in which  $v_{ave}$  is the annual average wind speed and taken as  $0.2v_{ref}$ .

**Table 6**  
Load cases according to (International Electrotechnical et al.).

DLC	Design situation	Wind		Wave		Analysis type	PSF
		Model	Speed	Model	Height		
1.1	Operating	NTM	$V_{in} < V_{hub} < V_{out}$	NSS	$E[H_s V_{hub}]$	U	1.35
6.1	Parked	EWM	$V_{hub} = V_{ref}$	ESS	$H_{s50}$	U	1.35
1.2	Operating	NTM	$V_{in} < V_{hub} < V_{out}$	NSS	Joint distribution	F	1.0

NTM: normal turbulent model; EWM: extreme wind speed model; NSS: normal sea state; ESS: extreme sea state; U: ultimate strength; F: fatigue strength; PSF: partial safety factor;  $V_{in}$ : cut-in wind speed;  $V_{out}$ : cut-out wind speed;  $V_{hub}$ : wind speed at hub;  $V_{ref}$ : reference wind speed with a recurrence period of 50 years;  $H_s$ : significant wave height;  $H_{s,ss}$ : significant wave height for severe sea state;  $H_{s50}$ : unconditional extreme significant wave height with a return period of 50 years..

In total 11 environmental states are applied to conduct the fatigue analysis with mean wind speeds from 5 m/s to 25 m/s, as shown Table 7. The combination of wind speed  $V_w$ , significant wave height  $H_s$  and peak wave period  $T_p$  correspond to a joint occurrence probability of  $P_j$ . All the combinations for the operational environmental states have a total probability of occurrence of 92%. Considering that the parked condition can have large contribution to the total fatigue damage as reported by Velarde et al. (2020), a wind turbine availability of 95% is assumed here. Thus, the fatigue estimation can consider both operational and parked conditions.

In addition, the wind and wave directionality is simplified by assuming the wind and wave loads are in the same direction, while yaw error is not considered in this study. To represent the influence of the OWT control, the relationship between the mean wind speed, rotor rotation speed and blade pitch angles shown in Fig. 8 was adopted

**Table 7**  
Environmental states, based on data from (Velarde et al., 2020).

Wind condition		Wave condition		
$V_w$ (m/s)	$I_n$ (%)	$T_p$ (s)	$H_s$ (m)	$P_j$ (%)
5	26.2	6.8	0.82	5.3
7	21.7	7.0	1.01	10.4
9	19.2	7.1	1.24	15.2
11	17.6	7.4	1.55	17.9
13	16.5	7.8	2.01	17.1
15	15.7	8.2	2.53	13.0
17	15.1	8.9	3.07	9.2
19	14.6	9.9	3.65	5.5
21	14.2	10.4	4.08	3.0
23	13.9	11.4	4.76	1.6
25	13.6	12.9	5.40	0.7
45.8	11.0	13.8	9.9	-

according to (Bak et al.). When the OWT is parked, it is assumed that the pitch angle is  $90^\circ$  with zero rotational speed.

#### 4.4. Modal properties and dynamic response analysis

##### 4.4.1. Natural frequencies and mode shapes

The natural frequencies of OWT towers should be kept far away from the resonance ranges caused by periodic wave loads and well known 1P and 3P rotor frequencies. Using the developed aeroelastic models, the natural frequencies of the hybrid tower are determined to be 0.25 Hz and 1.2 Hz for the first two bending modes in the FA direction. While for the reference tower, these two natural frequencies are 0.26 Hz and 1.37 Hz. The first natural frequencies are very close for both towers, while slight difference of the second mode is observed. Fig. 9 shows the 1P and 3P frequency ranging with a 10% safety margin together with the wave frequency ranging from 0.07 to 0.15 Hz. The natural frequencies of the hybrid tower and reference tower are both in the soft-stiff range and away from the rotor frequency and wave frequency ranges, indicating that the two towers are safe.

The mode shapes for the first and second tower bending modes of the hybrid tower are plotted in Fig. 10, and compared to those from the reference tower. It shows the mode shapes for the first and second bending modes of the two towers are also similar. As the modal properties of the hybrid tower and those of the reference tower are quite close, it can be concluded that the overall dynamic behaviour of these two towers should be also similar.

##### 4.4.2. Dynamics response analysis (deflection and acceleration)

The dynamic responses of the hybrid and reference towers were calculated given the wind and wave combinations defined in Table 7. For each mean wind speed, 6 random seeds were selected to generate the turbulent inflow wind fields and irregular wave profiles. A 650 s simulation was conducted for each random seed. Only the time series from 50 s to 650 s are used to evaluate the dynamic responses with the first 50 s simulation deducted as the initial transient responses. The representative displacement and acceleration responses for operating condition are plotted in Fig. 11, when the mean wind speed is 11 m/s which is close to the rated wind speed 11.4 m/s. As shown in Fig. 11, the tower top displacement in the FA direction fluctuates around 0.7 m, while the maximum tower top acceleration occurs in the FA direction and is less than  $0.6 \text{ m/s}^2$ . In this case, the thrust applied to the tower top as well as the displacement response reach their maximum values, since the OWT

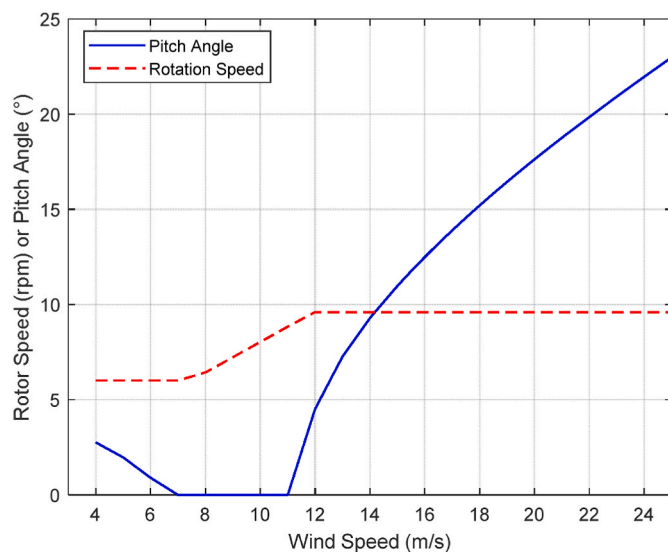


Fig. 8. Relationship between the rotor speed (dashed), pitch angle (solid) and inflow wind speed, based on (Bak et al.).

blades start to pitch when the wind speed is larger than the rated wind speed.

Additionally, the displacement and acceleration responses of the parked OWT under extreme condition with a mean wind speed of 45.8 m/s are shown in Fig. 12. Due to the large turbulence intensity and blade pitch angles of  $90^\circ$ , the displacements and accelerations in the FA and SS directions have both large amplitudes and significant fluctuations. The tower top displacement is under 0.8 m, and acceleration is below  $1.3 \text{ m/s}^2$ .

Although there is no general agreement on wind turbine tower deflection design limit, the latest Chinese standard (China Electricity Council, 2018) for prestressed precast concrete wind turbine tower sets a limit for the deflection of the wind turbine tower top as 1% of the tower length. According to time domain simulation results, the maximum displacement of the hybrid tower top is 0.9 m, which is below the limit (1.49 m). On the other hand, it is common to set a limit for the maximum acceleration on the tower top, and this limit is in the range of 0.15 g–0.3 g (China Electricity Council, 2018; Nejad et al., 2016). The tower top acceleration reaches the maximum value of  $1.2 \text{ m/s}^2$  when the OWT is exposed to the extreme wind as shown in Fig. 12(b). This maximum acceleration is also less than the acceleration limit. So, it can be concluded that the design of the hybrid tower satisfies the design requirements for tower top deflection and acceleration.

#### 4.5. Ultimate resistance checking

As an OWT tower can be regarded as a cantilever supported by soil springs at the mudline (Adhikari and Bhattacharya, 2012), the largest moment can be usually found at the bottom section at the mudline. Although it is possible that the moment can reach its maximum value below the mudline (Rezaei et al., 2018), this paper assumes the maximum moment occurs at the section at the mudline for the purpose of a feasibility study.

The ultimate design moments are determined by the numerical simulations (as described in Section 4.4.2) for DLC1.1 and DLC6.1 considering different combinations of winds and waves and random seeds. Given a mean wind speed and a random seed, the maximum bending moments at the tower bottom section are obtained from the time series of internal forces. For each mean wind speed, the mean value and standard deviation are calculated from the maximum bending moments corresponding to the 6 random seeds. Fig. 13 compares the calculated mean values and standard deviations of the maximum bending moments between the hybrid tower and reference tower under different mean wind speeds. It can be observed that the maximum bending moments are generally similar for both tower structures. When the OWTs are operating at the rated wind speed, the mean value and standard deviation of the maximum bending moments are 429 MN m and 11 MN m for the hybrid tower, which are slightly smaller than those (433 MN m and 13 MN m, respectively) for the reference tower. The maximum bending moments become smaller for other mean wind speeds. When the OWTs are parked and subjected to extreme wind, the mean value and standard deviation of the maximum bending moment for the hybrid tower are 433 MN m and 42 MN m, which are slightly smaller than those for the reference tower.

To calculate the ultimate resistance of the reinforced UHPFRC section and the steel tube section, it first requires determining the axial loading. According to the simulation results for DLC1.1 and DLC6.1, the axial loading slightly fluctuates around the total gravitational load caused by the rotor-nacelle assembly (RNA) mass and tower mass. Thus, the design axial loading can be regarded as the total gravitational load. By using the estimation methods given in Section 3.3, the calculated ultimate strength for the reinforced UHPFRC tube section at the mudline is 549 MN m. For the reference tower, and the ultimate strength of the steel tube section at the mudline is 1545 MN m by using the method detailed in Appendix A.

According to all the simulation results, the maximum design moment

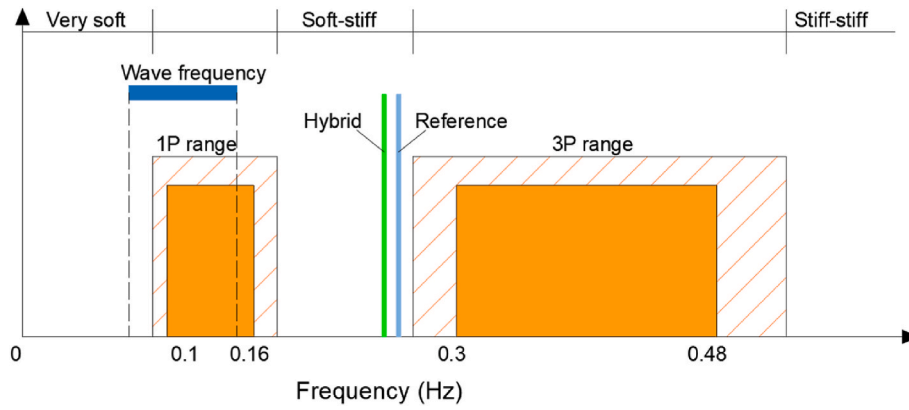


Fig. 9. Frequency ranges and natural frequencies.

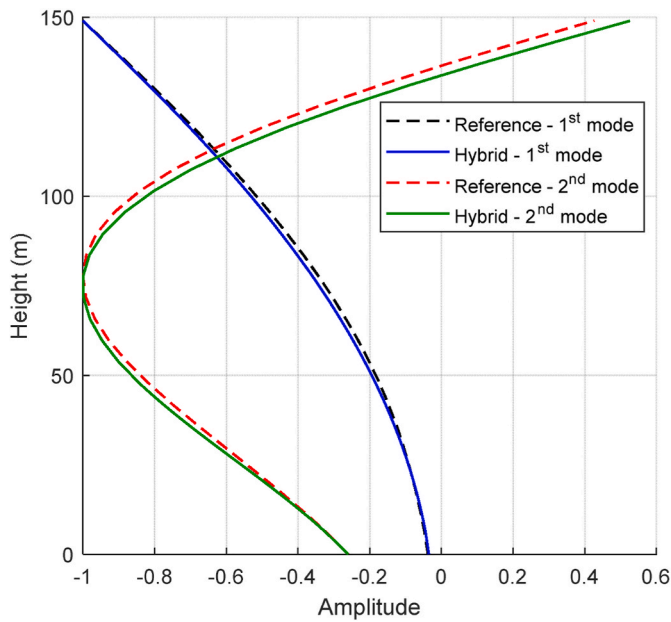


Fig. 10. Mode shapes for the first and second bending modes of the hybrid and reference towers.

for the hybrid tower is 473 MN m which is less than the ultimate resistance of 549 MN m. Similar result is observed for the steel reference tower, while its ultimate resistance is around 2 times higher than the design moment. It is widely known that the design of steel OWT towers is more dependent on their fatigue resistance (Rezaei et al., 2018). Thus,

it cannot be concluded that the reference steel tower in this paper is oversized given its large ultimate strength.

#### 4.6. Fatigue life prediction

Similarly, the fatigue life prediction of the towers are conducted on the tube section at the mudline. The time domain simulations conducted for DLC1.1 can also be used to conduct fatigue analysis for DLC1.2 as the combinations of winds and waves are the same in both load cases. Given the axial force  $F_z$ , bending moments  $M_x$  and  $M_y$ , the longitudinal stress at an arbitrary position  $(x, y)$  at the tube section can be obtained:

$$\sigma_{zz}(x, y) = \frac{F_z}{A} + \frac{M_x}{I_x}y - \frac{M_y}{I_y}x, \quad (21)$$

where  $I_x$  and  $I_y$  are the second moment of area about  $x$  and  $y$  axes respectively,  $A$  is the section area. Equation (21) is only used when loads applied to the tube section are relatively low and the strain-stress relationships of UHPFRC and steel are in the elastic stage. To consider material nonlinearity, the method provided in Section 3.3 is used to calculate the stresses of the tube section, when the loads on the section are so large that the UHPFRC is the hardening stage or the steel is the plastic stage.

For the reinforced UHPFRC section, all the rebars are located at the middle of the circular section for simplicity and the stress distribution for the UHPFRC and rebars are considered by assuming a linear strain distribution along the section. For the tube section of the hybrid tower at the mudline, the maximum tensile stress time histories at the section edge are shown in Fig. 14(a) for representative mean wind speeds of 5, 11, 19 and 25 m/s and random seed 1, and the maximum tensile stress time histories in rebars are plotted in Fig. 14(b). It can be observed that the maximum tensile stresses on the edge of the reinforced UHPRC

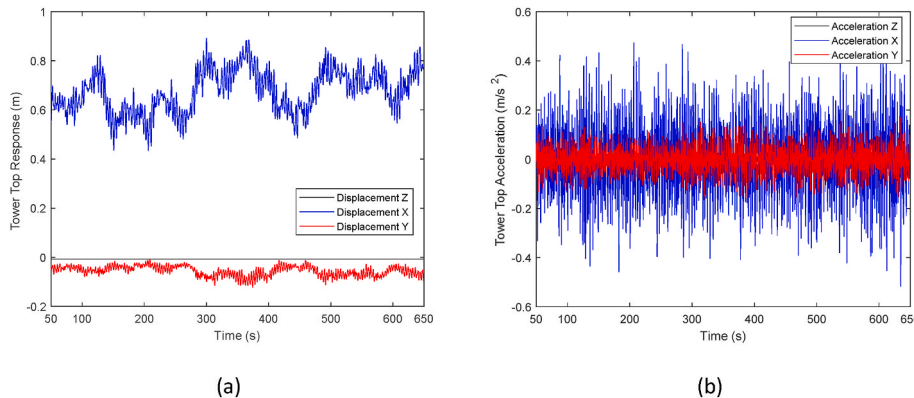


Fig. 11. Tower top displacement (a) and acceleration (b) responses of the hybrid tower under operating condition with a mean wind speed of 11 m/s.

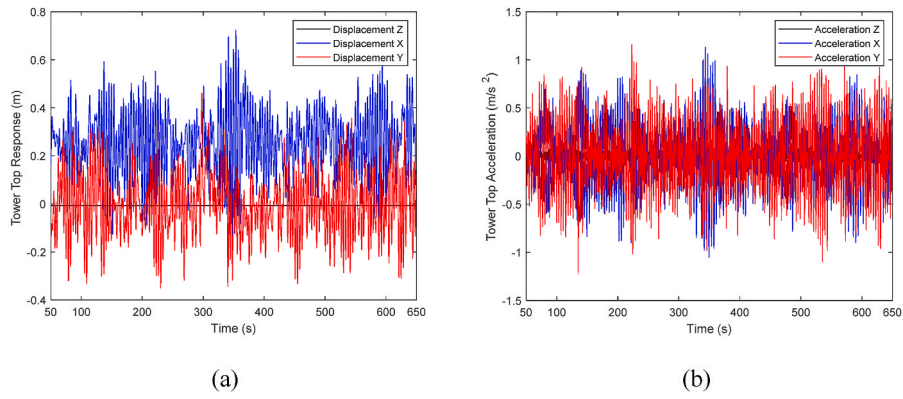


Fig. 12. Tower top displacement (a) and acceleration (b) responses of the hybrid tower for parked condition with a mean wind speed of 45.8 m/s.

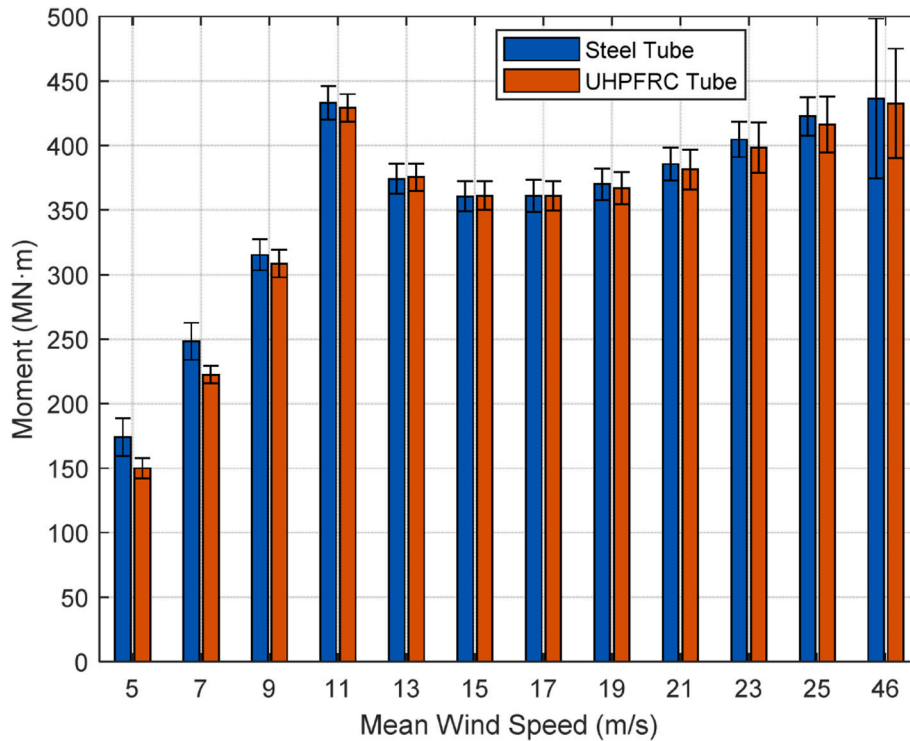


Fig. 13. Mean values and standard deviations of the maximum bending moments at the mudline for the hybrid tower and reference tower.

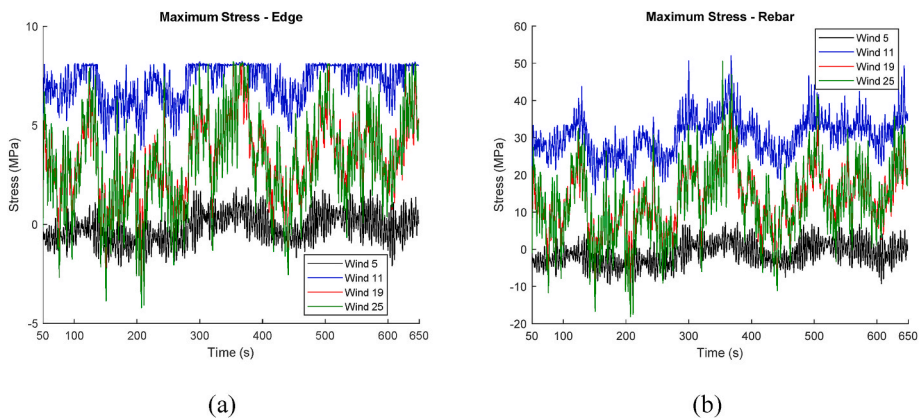


Fig. 14. Maximum tensile stress time histories on the edge of the reinforced UHPFRC tube section (a) and in the rebars (b).

section are almost all below elastic limit of UHPFRC material ( $<8$  MPa) at various wind speeds except for the wind speed of 11 m/s, where the maximum stress is slightly higher than 8 MPa. These stress levels are still under the fatigue endurance limit of UHPFRC as validated experimentally by the authors' previous work (Shen and Brühwiler, 2020b), implying no risk of fatigue failure of UHPFRC. For steel rebar, the maximum stresses are all less than 55 MPa, which is far below the fatigue endurance limit of steel (115 MPa when the number of cycles is above  $10^8$ ). It is deserved to mention that more stress is transferred from UHPFRC to steel rebar once the UHPFRC enters in strain-hardening domain ( $>8$  MPa), retarding further stress increase and thus damage propagation of UHPFRC. Similar phenomenon was reported by Makita et al. (Makita and Brühwiler, 2014a).

For each mean wind speed, the mean value and standard deviation of the maximum stress ranges for UHPFRC and rebars can be obtained from the stress time series given 6 random seeds. These maximum stress ranges are illustrated in Fig. 15, showing that the maximum stress range increases with the increase of mean wind speed. The averaged maximum stress range for rebars grows from 20.4 MPa to 68.8 MPa when the mean wind speed changes from 5 m/s to 25 m/s. According to the tensile fatigue S–N curve of rebars given in Fig. 6 and the stresses ranges corresponding to different mean wind speeds and random seeds, the fatigue damage index for each 600 s stress time history can be obtained. Then the fatigue life of the UHPFRC tube can be predicted through the fatigue life calculation method described in Section 3.4. Results show that the fatigue life of the UHPFRC tube in the hybrid tower can be up to  $1.3 \times 10^7$  years, implying no fatigue issue exists. Similar result is obtained for the compressive fatigue checking of UHPFRC (the maximum compressive stress range is 15.6 MPa).

For the reference steel tube section at the mudline, the stress time histories at the section edge are shown in Fig. 16(a) with different mean wind speeds. The mean value and standard deviation of the maximum stress ranges for the reference steel tube section were also calculated and given in Fig. 16(b). With the simulation results for DLC1.2, the fatigue life predictions can be done for the reinforced UHPFRC tube section in the hybrid tower based on different curves, and for the steel tube section in the reference tower. Combining the fatigue damage summing rule given in Eq. (15) and the occurrence probability for each mean wind speed, the fatigue life of the reference steel tower is predicted to be 55.7 year.

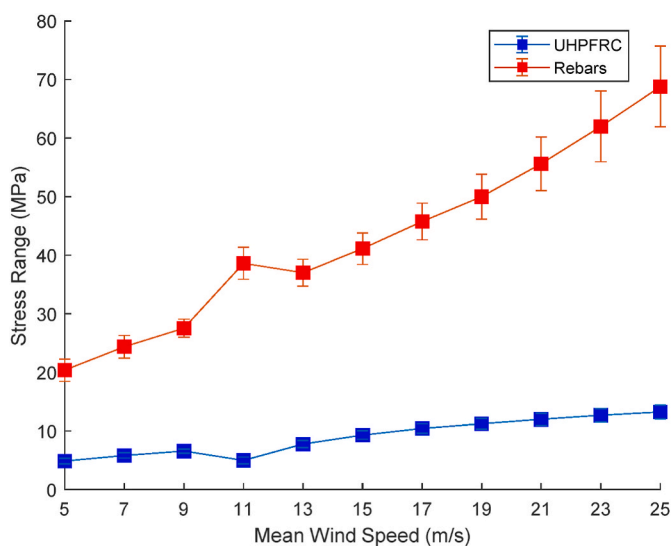


Fig. 15. Maximum stress ranges for UHPFRC and rebars with different mean wind speeds.

#### 4.7. Cost estimation

In general, costs for the hybrid tower include those for materials, fabrication, transport, installation and maintenance. The costs for materials are relatively easy to calculate, but it is difficult to accurately estimate the costs for installation, manufacturing, and transport (Ma and Yang, 2020). Here only the total material cost for the hybrid tower and reference tower are estimated and compared. The price of steel is set as 10000 ¥/ton including the costs for raw material and labour, while the price of UHPFRC is set as 2500 ¥/ton, following the price ranges for steel and UHPFRC given in (Ma and Yang, 2020). The influence of the connections throughout the tower structure is on the cost ignored here. The calculated material masses and material prices for the reinforced UHPFRC tube and the reference steel tube are listed in Table 8. It shows that the total material cost of the hybrid tower is  $11 \times 10^6$  ¥, which is only 58% of that of the reference steel tube tower. It should be noted that the cost of hybrid tower will be further reduced considering the higher durability and less requirement of protective measures. Furthermore, it can be found that the mass of hybrid tower is comparable to that of reference steel tower.

#### 5. Conclusions

The present study proposes a steel-UHPFRC hybrid tower structure with height of 149 m above the mudline to support a 10 MW DTU reference OWT. The sectional analysis method considering the tensile properties of UHPFRC materials is developed to determine the ultimate strength of the reinforced UHPFRC tube section, and the fatigue strength of this section is evaluated based on rain-flow counting and S–N curves of materials. The ultimate and fatigue strengths of the reinforced UHPFRC tube are studied under different operational and environmental conditions, and the results are compared with those from a reference steel tube. The main conclusions are presented as follows:

- 1) The natural frequencies of the hybrid tower are determined to be 0.25 Hz and 1.2 Hz for the first two bending modes, which are close to those of the reference steel tower. And the mode shapes from both towers are close.
- 2) The maximum displacement and acceleration responses of the hybrid tower at top are 0.9m and  $1.2 \text{ m/s}^2$ , which are both under the design limits.
- 3) The ultimate strength for the reinforced UHPFRC tube section at the mudline is 549 MN m meeting the design requirement (473 MN m), while it is much smaller than that from the reference steel tower (1545 MN m).
- 4) The maximum fatigue tensile stresses of both UHPFRC and steel rebars are both under fatigue endurance limits, leading to much longer fatigue life of the hybrid tower compared with that of the reference tower.
- 5) The total material cost of the hybrid tower is 58% of that from the reference steel tower, while the masses of both towers are comparable.

In the present study, a linear dynamic model together with an ultimate strength calculation method which assumes a linear strain distribution of the UHPFRC tube section are used. It should be note that these approaches ignore the nonlinearity in structural behaviour, which may lead to inaccurate results for dynamic responses and stress predictions when the section loads are too large. However, the precision of the linear model used in this study can be sufficient for a preliminary feasibility study. In the future, more accurate models will be used to better consider the geometric and material nonlinearities and the influence of connections.

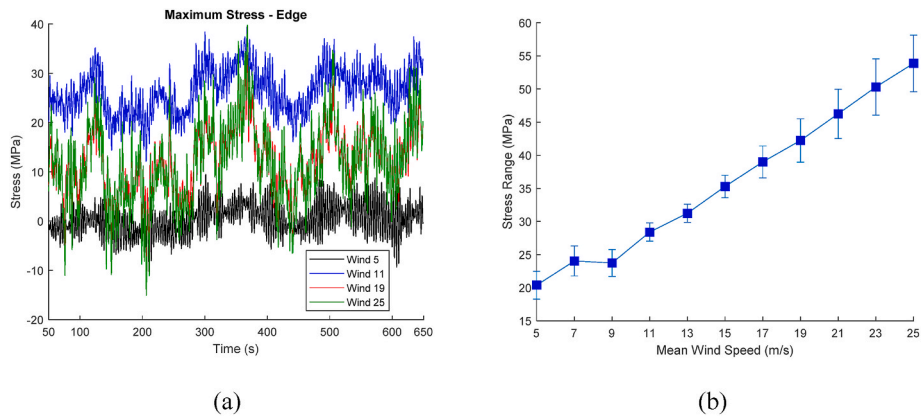


Fig. 16. Maximum tensile stress time series for the steel tube section at the mudline (a) and the corresponding maximum stress ranges with different mean wind speeds (b).

Table 8

Masses and prices of the reinforced UHPFRC tube and reference steel tube.

Reinforced UHPFRC tube		Reference steel tube	
UHPFRC tube mass (t)	1804	Steel tube mass (t)	1872
Steel tube mass (t)	587	Steel price (¥)	$19 \times 10^6$
Rebar mass (t)	63		
UHPFRC price (¥)	$4.5 \times 10^6$		
Steel price (¥)	$6.5 \times 10^6$		
Total price (¥)	$11 \times 10^6$	Total price (¥)	$19 \times 10^6$

#### CRedit authorship contribution statement

**Chao Chen:** Writing – original draft, preparation, Data curation, Conceptualization, Methodology, and, Software. **Xiujiang Shen:** Conceptualization, Writing – review & editing, and, Data curation. **Zheng Zhou:** Investigation, and, Validation. **Xugang Hua:** Investigation.

#### Appendix A

To determine the ultimate strength of the steel tube with a radius of  $r$  and thickness of  $t$ , the buckling resistance calculation method recommended by DNVGL (DNVGL, DNVGL-RP-C202, 2019) for a cylindrical shell can be used. If only considering the stresses caused by the axial force  $F_z$  and ultimate bending moment  $M_u$ , the design axial stress  $\sigma_a$  and bending stress  $\sigma_m$  should satisfy the stability requirement given by:

$$\sigma_a + \sigma_m = \frac{F_z}{A} + \frac{M_u}{W} = \frac{f_y}{\gamma_m \sqrt{1 + \bar{\lambda}_s^4}} \quad (\text{A. 1})$$

where  $A$  is the section area,  $W$  is the elastic section modulus,  $f_y$  is the steel yield stress.  $\bar{\lambda}_s$  is the reduced shell slenderness and can be determined by

$$\bar{\lambda}_s^2 = \frac{f_y}{f_E}, \quad (\text{A. 2})$$

where  $f_E$  is the elastic buckling strength for axial force or bending moment.  $f_E$  can be calculated by

$$f_E = C \frac{\pi^2 E}{12(1 - \nu^2)} \left(\frac{t}{l}\right)^2, \quad (\text{A. 3})$$

where  $E$  is Young's modulus,  $\nu$  is Poisson's ratio,  $l$  is the effective shell length.  $\gamma_m$  is a material factor and can be calculated as:

$$\gamma_m = \begin{cases} 1.15 & \text{for } \bar{\lambda}_s < 0.5 \\ 0.85 + 0.60 & \text{for } 0.5 \leq 1.0 \bar{\lambda}_s \leq 1.0 \\ 1.45 & \text{for } \bar{\lambda}_s > 1.0 \end{cases} \quad (\text{A. 4})$$

The reduced buckling coefficient  $C$  can be calculated by

#### Declaration of competing interest

The authors declare that they have no known competing financial interests or personal relationships that could have appeared to influence the work reported in this paper.

#### Data availability

No data was used for the research described in the article.

#### Acknowledgement

The financial supports from the National Natural Science Foundation of China (No. 52108280, No. 52108138) and the National Science Fund for Distinguished Young Scholars (No. 52025082) are greatly appreciated.

$$C = \psi \sqrt{1 + \left(\frac{\rho \xi}{\psi}\right)^2}, \quad (\text{A. 5})$$

where  $\psi = 1$ ,  $\xi = 0.702Z_l$ ,  $\rho = 0.5\left(1 + \frac{r}{150r}\right)^{-0.5}$ .  $Z_l$  can be determined by

$$Z_l = \frac{r^2}{rt} \sqrt{1 - \nu^2} \quad (\text{A. 6})$$

As the axial force is mainly caused by gravity loads and its fluctuation is relatively insignificant, a constant axial stress can be assumed when calculating the ultimate bending moment. Given a known axial force, the ultimate bending stress  $\sigma_m$  can be found from Equation (A. 1). Then the ultimate bending resistance is obtained by  $M_u = \sigma_m W$ .

## References

- Adhikari, S., Bhattacharya, S., 2012. Dynamic analysis of wind turbine towers on flexible foundations. *Shock Vib. Digest* 19, 37–56.
- Bak C, Zahle F, Bitsche R, et al. Description of the DTU 10 MW Reference Wind Turbine.. Benjamin, Graybeal, Eugen, Brühwiler, Kim, Byung-Suk, et al., 2020. International perspective on UHPC in bridge engineering. *J. Bridge Eng.* 25, 04020094.
- Brühwiler, E., 2020. UHPFRC technology to enhance the performance of existing concrete bridges. *Struct. Infrastruct. Eng. Maint., Manag. Life-Cycle Des. Perform.* 16, 94–105.
- Chen, C., Duffour, P., 2018. Modelling damping sources in monopile-supported offshore wind turbines. *Wind Energy* 21, 1121–1140.
- Chen, Y., Yu, R., Wang, X., et al., 2018. Evaluation and optimization of ultra-high performance concrete (UHPC) subjected to harsh ocean environment: towards an application of layered double hydroxides (LDHs). *Construct. Build. Mater.* 177, 51–62.
- Chen, C., Duffour, P., Fromme, P., et al., 2021. Numerically efficient fatigue life prediction of offshore wind turbines using aerodynamic decoupling. *Renew. Energy* 178, 1421–1434.
- Chen, C., Duffour, P., Fromme, P., et al., 2023. Simplified complex-valued modal model for operating wind turbines through aerodynamic decoupling and multi-blade coordinate transformation. *J. Sound Vib.* 547, 117512.
- China Electricity Council, 2018. Code of Prestressed Precast Concrete Tower for Wind Turbine. China Electricity Council.
- Damiani RR. 10 - design of offshore wind turbine towers. In: Ng C, Ran L (eds) *Offshore Wind Farms*. Woodhead Publishing, pp. 263–357..
- Darvishi-Alamouti, S., Bahaari, M.-R., Moradi, M., 2017. Natural frequency of offshore wind turbines on rigid and flexible monopiles in cohesionless soils with linear stiffness distribution. *Appl. Ocean Res.* 68, 91–102.
- (DNV) Det Norske Veritas. DNV-RP-C203: Fatigue Design of Offshore Steel Structures. DNVGL. DNVGL-RP-C202, 2019. Buckling Strength of Shells. DNVGL-RP-C202.
- GWEC, 2022. Global Offshore Wind Report 2022.
- Hansen, M.O.L., 2015. *Aerodynamics of Wind Turbines*, third ed. Routledge, London, England.
- Hasselmann, K., Barnett, T.P., Bouws, E., et al., 1973. Measurements of wind-wave growth and swell decay during the joint North Sea wave project (JONSWAP). *Ergänzungsheft zur Deutschen Hydrographischen Zeitschrift Reihe A (8)*, 1–95.
- Huang, X., Li, B., Zhou, X., et al., 2022. Geometric optimisation analysis of Steel-Concrete hybrid wind turbine towers. *Structures* 35, 1125–1137.
- International Electrotechnical Commission (IEC). IEC 61400-3 Wind Turbines - Part 3: Design Requirements for Offshore Wind Turbines..
- Jammes, F.-X., 2009. Design of Wind Turbines with Ultra-high Performance Concrete. Massachusetts Institute of Technology.
- Jammes, F.-X., Cespedes, X., Resplendino, J., 2013. Design of offshore wind turbines with UHPC. In: RILEM-fib-AFGC Int. Symposium on Ultra-high Performance Fibre-Reinforced Concrete, pp. 443–452.
- Jonkman, J.M., Buhl Jr., M.L., 2005. FAST User's Guide. National Renewable Energy Laboratory, Golden, CO, USA. Technical Report NREL/EL-500-38230.
- Lewin, T.J., 2010. An Investigation of Design Alternatives for 328-ft (100-m) Tall Wind Turbine Towers, p. 192.
- Loraux, C.T., 2018. Long-term Monitoring of Existing Wind Turbine Towers and Fatigue Performance of UHPFRC under Compressive Stresses. Ecole Polytechnique Fédérale de Lausanne.
- Ma, H., Yang, J., 2020. A novel hybrid monopile foundation for offshore wind turbines. *Ocean Eng.* 198, 106963.
- Makita, T., 2014. Fatigue Behaviour of UHPFRC and R-UHPFRC-RC Composite Members. Ecole Polytechnique Fédérale de Lausanne.
- Makita, T., Brühwiler, E., 2014a. Tensile fatigue behaviour of ultra-high performance fibre reinforced concrete (UHPFRC). *Mater. Struct.* 47, 475–491.
- Makita, T., Brühwiler, E., 2014b. Tensile fatigue behaviour of ultra-high performance fibre reinforced concrete combined with steel rebars (R-UHPFRC). *Int. J. Fatig.* 59, 145–152.
- Mathern, A., von der Haar, C., Marx, S., 2021. Concrete support structures for offshore wind turbines: current status, challenges, and future trends. *Energies* 14, 1995.
- Musial, W., Spitsen, P., Duffy, P., et al., 2022. Offshore Wind Market Report: 2022 Edition. NREL/TP-5000-83544. National Renewable Energy Lab. (NREL), Golden, CO (United States). August 11.
- Nejad, A.R., Bachynski, E.E., Li, L., et al., 2016. Correlation between acceleration and drivetrain load effects for monopile offshore wind turbines. *Energy Proc.* 94, 487–496.
- Peggar, R., 2017. Design and Structural Testing of Tall Hexcrete Wind Turbine Towers. Ph.D. Thesis. Iowa State University.
- Price, S.J., Figueira, R.B., 2017. Corrosion protection systems and fatigue corrosion in offshore wind structures: current status and future perspectives. *Coatings* 7, 25.
- Rezaei, R., Fromme, P., Duffour, P., 2018. Fatigue life sensitivity of monopile-supported offshore wind turbines to damping. *Renew. Energy* 123, 450–459.
- Riccio, A., Saputo, S., Sellitto, A., 2016. A user defined material model for the simulation of impact induced damage in composite. *Key Eng. Mater.* 713, 14–17.
- Shabani, P., Shabani, N., 2022. Fatigue life prediction of high-speed composite craft under slamming loads using progressive fatigue damage modeling technique. *Eng. Fail. Anal.* 131, 105818.
- Shen, X., Brühwiler, E., 2020a. Influence of local fiber distribution on tensile behavior of strain hardening UHPFRC using NDT and DIC. *Cement Concr. Res.* 132, 106042.
- Shen, X., Brühwiler, E., 2020b. Biaxial flexural fatigue behavior of strain-hardening UHPFRC thin slab elements. *Int. J. Fatig.* 138, 105727.
- Shirzadeh, R., Devriendt, C., Bidakvidi, M.A., et al., 2013. Experimental and computational damping estimation of an offshore wind turbine on a monopile foundation. *J. Wind Eng. Ind. Aerod.* 120, 96–106.
- Sritharan, S., Lewin, T.J., 2015. Wind Turbine Tower System, 9016012.
- Sritharan, S., Schmitz, G.M., 2013. Design of tall wind turbine towers utilizing UHPC. RILEM-fib-AFGC Int. Sympos. Ultra-High Perform. Fibre-Reinforc. Concrete 433–442.
- Swiss Society of Engineers and Architects, 2016. Technical Leaflet SIA 2052 UHPFRC – Materials, Design and Construction. Swiss Society of Engineers and Architects.
- Toader T-N, Schmeer D, Sobek W. Concept for an onshore tower structure made of UHPFRC segments for wind turbines. *Acta Technica Napocensis: Civil Eng. Architect.*; 62..
- Uys, P.E., Farkas, J., Jármai, K., et al., 2007. Optimisation of a steel tower for a wind turbine structure. *Eng. Struct.* 29, 1337–1342.
- Velarde, J., Kramhøft, C., Sørensen, J.D., et al., 2020. Fatigue reliability of large monopiles for offshore wind turbines. *Int. J. Fatig.* 134, 105487.
- Veldkamp, H.F., Tempel, J.V.D., 2005. Influence of wave modelling on the prediction of fatigue for offshore wind turbines. *Wind Energy* 8, 49–65.
- Wang, S., Larsen, T.J., Bredmose, H., 2021. Ultimate load analysis of a 10 MW offshore monopile wind turbine incorporating fully nonlinear irregular wave kinematics. *Mar. Struct.* 76, 102922.
- Wu, X., Yang, J., Mpalla, I.B., 2013. Preliminary design and structural responses of typical hybrid wind tower made of ultra high performance cementitious composites. *Struct. Eng. Mech. : Int. J.* 48, 791–807.
- Yang, Y., Bashir, M., Li, C., et al., 2020. Mitigation of coupled wind-wave-earthquake responses of a 10 MW fixed-bottom offshore wind turbine. *Renew. Energy* 157, 1171–1184.
- Zhai, G., Wei, Z., Ma, Z., et al., 2023. Establishment and program development of failure criterion of hollow glass microspheres/epoxy resin composites based on tension/compression discrepancy. *Eng. Fail. Anal.* 149, 107270.